Monthly Notices of the ROYAL ASTRONOMICAL SOCIETY

MNRAS **531,** 617–631 (2024) https://doi.org/10.1093/mnras/stae964
Advance Access publication 2024 May 16

EPOCHS Paper – VIII. An insight into MIRI-selected galaxies in SMACS-0723 and the benefits of deep MIRI photometry in revealing AGN and the dusty universe

Qiong Li [1]★ Christopher J. Conselice [1] Nathan Adams [1] James A. A. Trussler [1] Duncan Austin [1] Thomas Harvey [1] Leonardo Ferreira [2] Joseph Caruana [3,4] Katherine Ormerod [1] and Ignas Juodžbalis [5,6]

[1] *Jodrell Bank Centre for Astrophysics, University of Manchester, Oxford Road, Manchester, M13 9PL, UK*
[2] *Department of Physics & Astronomy, University of Victoria, , Finnerty Road, Victoria, British Columbia, V8P 1A1, Canada*
[3] *Department of Physics, University of Malta, Msida MSD 2080, Malta*
[4] *Institute of Space Sciences & Astronomy, University of Malta, Msida MSD 2080, Malta*
[5] *Kavli Institute for Cosmology, University of Cambridge, Madingley Road, Cambridge CB3 0HA, UK*
[6] *Cavendish Laboratory, University of Cambridge, 19 JJ Thomson Avenue, Cambridge CB3 0HE, UK*

Accepted 2024 April 3. Received 2024 March 2; in original form 2023 September 14

ABSTRACT

We present the analysis of the stellar population and star formation history of 181 MIRI selected galaxies at $z = 0 - 3.5$ in the massive galaxy cluster field SMACS J0723.3–7327, commonly referred to as SMACS0723, using the JWST Mid-Infrared Instrument (MIRI). We combine the data with the JWST Near Infrared Camera (NIRCam) catalogue, in conjunction with the Hubble Space Telescope (HST) WFC3/IR and ACS imaging. We find that the MIRI bands capture PAH features and dust emission, significantly enhancing the accuracy of photometric redshift and measurements of the physical properties of these galaxies. The median photo-z's of galaxies with MIRI data are found to have a small 0.1 per cent difference from spectroscopic redshifts and reducing the error by 20 per cent. With MIRI data included in SED fits, we find that the measured stellar masses are unchanged, while the star formation rate is slightly lower by 0.1 dex. We also fit the median SED of active galactic nuclei (AGNs) and star-forming galaxies (SFG) separately. MIRI data provides tighter constraints on the AGN contribution, reducing the typical AGN contributions by ∼15 per cent. In addition, we also compare the median SED obtained with and without MIRI, and we find that including MIRI data yields steeper optical and UV slopes, indicating bluer colours, lower dust attenuation, and younger stellar populations. In the future, MIRI/MRS will enhance our understanding by providing more detailed spectral information and allowing for the study of specific emission features and diagnostics associated with AGN.

Key words: galaxies: formation – galaxies: general – galaxies: photometry – galaxies: star formation.

1 INTRODUCTION

In the vast expanse of the universe, many galaxies remain hidden behind a veil of dust, rendering them challenging to observe using traditional optical telescopes (e.g. Asboth et al. 2016; Fudamoto et al. 2017; Reuter et al. 2020). Dust particles can absorb or scatter the emitted light, obstructing our view and limiting our understanding of their properties and evolution. However, the advent of the JWST and its successful commissioning have opened up a new era of exploration at infrared wavelengths (Menzel et al. 2023; Rigby et al. 2023).

JWST has started to revolutionize our ability to study the dusty universe by enabling deep imaging and spectroscopy in the 1–30 μm wavelength range. Its new capabilities, including high sensitivity and exceptional spatial resolution, have propelled our investigations into the basic features of galaxies (e.g. Castellano et al. 2022; Harikane et al. 2022; Naidu et al. 2022; Pontoppidan et al. 2022; Adams et al. 2023; Yan et al. 2023). By delving deep into the universe with this imaging, we can uncover intricate details about galaxy structures, stellar populations, and the interplay between stars, gas, and dust. Furthermore, the JWST's infrared observations provide valuable insights into star formation processes, dust distribution, and the activity of supermassive black holes at the centers of galaxies.

The emission from dust in the star-forming galaxies (SFGs) can be divided into three components as wavelength increases towards the red. The dominant features observed in the ∼ 3–20 μm mid-infrared range are attributed to polycyclic aromatic hydrocarbon (PAH) bands, as discussed in studies such as (Allamandola, Tielens & Barker 1989; Li & Draine 2001; Draine & Li 2007; Li 2020). These PAHs can absorb UV photons and re-emit the absorbed energy as fluorescence at longer wavelengths, typically in the mid-infrared range (e.g. sometimes known as 'Sellgren Grains', dust grains size $a \sim 10$ Å and temperate peak $T \sim 1000$ K in Sellgren, Werner & Dinerstein 1983). As the wavelength increases to the mid-infrared range, the emission is progressively taken over by very small, warm grains. At higher

★ E-mail: qiong.li@manchester.ac.uk

© 2024 The Author(s).
Published by Oxford University Press on behalf of Royal Astronomical Society. This is an Open Access article distributed under the terms of the Creative Commons Attribution License (https://creativecommons.org/licenses/by/4.0/), which permits unrestricted reuse, distribution, and reproduction in any medium, provided the original work is properly cited.

Downloaded from https://academic.oup.com/mnras/article/531/1/617/7675333 by Liverpool John Moores University user on 23 September 2024

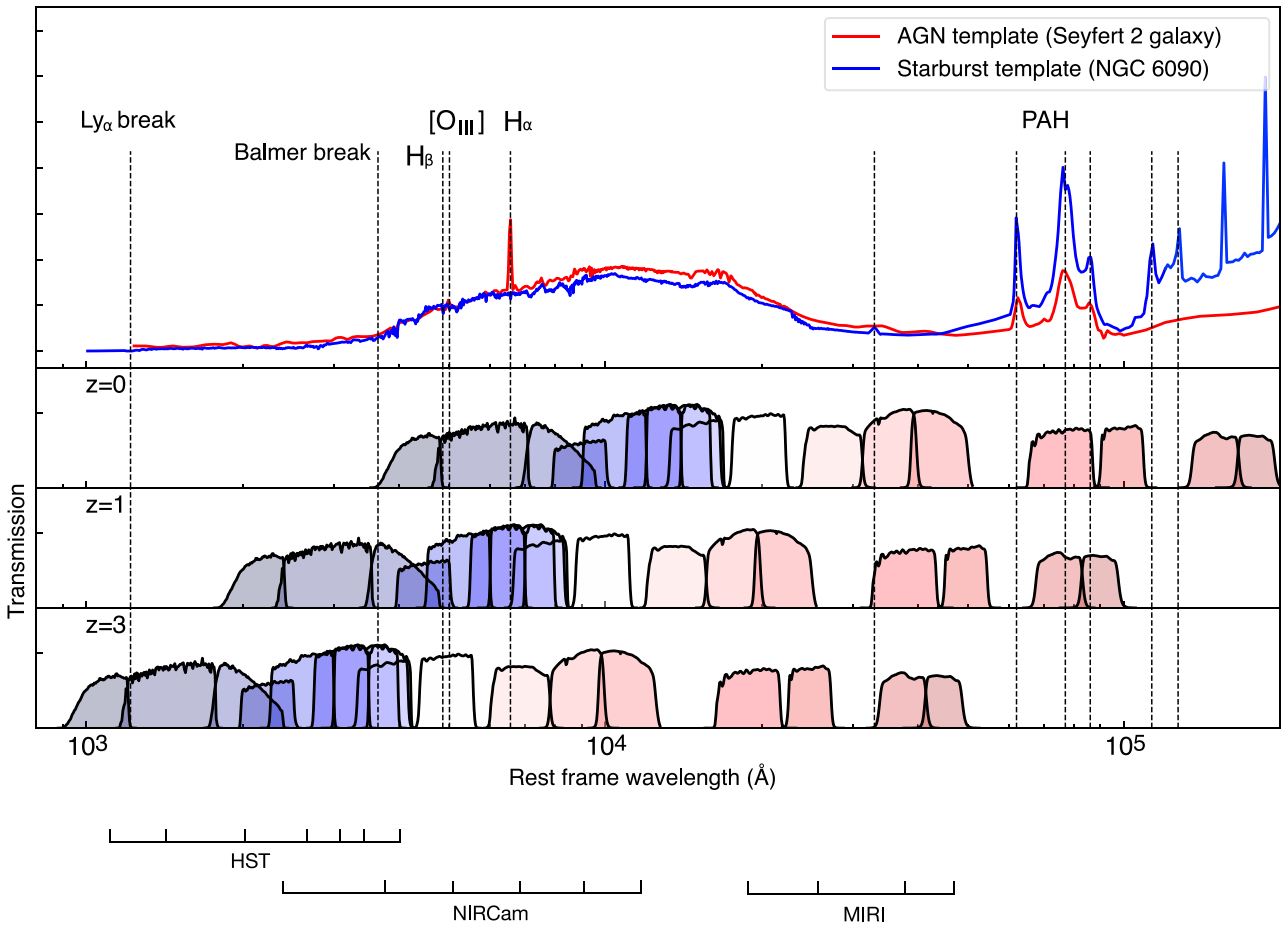

Figure 1. Plot showing the JWST and HST filters we use as well as SEDs for representative AGNs and SFGs. The broadband coverage of the AGN (Seyfert 2 galaxy) and starburst galaxy (NGC6090) templates (λF_λ, in relative units of erg s^{-1}) at different redshift bins (Weedman et al. 2006) are shown. The top panel presents the AGN and star-forming galaxy templates, while the bottom panel displays the relative transmission functions for various filters: HST/ACS and WCS3/IR (F435W, F606W, F814W, F105W, F125W, F140W, and F160W), JWST/NIRCam (F090W, F150W, F200W, F277W, F356W, and F444W), and JWST/MIRI (F770W, F1000W, F1500W, and F1800W). Emission lines and PAH features are appropriately labelled. Notably, the MIRI data enable us to probe the SEDs of galaxies up to ~ 5 μm (at $z \sim 2$–3) in the rest-frame, facilitating the characterization of PAH features and dust emission.

radiation field intensities, the thermal continuum emission from non-equilibrium heating of warm grains becomes dominant and reaching temperatures from a few hundred to a few thousand K (Draine 2003). Beyond 100 μm, the emission is increasingly attributed to larger, relatively cold grains with the grain size exceeding 0.01 μm and emit at temperatures $T \sim 30$–100 K (e.g. Ysard et al. 2019; McKay et al. 2023).

While the *Spitzer* Space Telescope allowed observations in this mid-infrared range, it had severe limitations in sensitivity and resolution at longer wavelengths (e.g. Ashby et al. 2015; Timlin et al. 2016; Nayyeri et al. 2018). The JWST's Mid-Infrared Instrument (MIRI; Rieke et al. 2015) has made significant advancements over this, offering higher sensitivity at a magnitude limit as deep as ∼29 mag (and perhaps beyond) and with sub-arcsec resolution (Rigby et al. 2023; Wright et al. 2023). The advanced capabilities of MIRI thus enable more precise investigations into the impact of dust on star formation and galaxy evolution, as well as the analysis of PAH features in the mid-infrared (see Fig. 1), surpassing the limitations of optical and earlier infrared observations. In principle, longer wavelengths can be used to find AGN and this is another advantage that MIRI has over what can be carried out with just NIRCam to find and characterize these objects, although see Yang et al. (2021); Juodžbalis et al. (2023). Recently, Lyu et al. (2023) reported 217 MIRI-selected AGNs from SMILES, a JWST Cycle 1 GTO program, in the GOODS-S field, covering ∼34 arcmins^2. Notably, 34 per cent of the AGNs do not have previous identifications. Yang et al. (2023) also discovered 25 MIRI-selected AGNs at $z = 0$–5 in the CEERS field. The spectral energy distributions (SEDs) of these AGNs closely resemble typical SEDs observed in hot dust-obscured galaxies and Seyfert 2 galaxies. Kirkpatrick et al. (2023) point out that MIRI excels in detecting faint galaxies with $L_{IR} < 10^{10} L_\odot$ at $z = 1$–2, and thus find <10 infrared AGNs per MIRI pointing. Likewise, Barro et al. (2024) investigate 37 Extremely Red Galaxies at $z = 5$–9 using MIRI and NIRSpec, suggesting that these galaxies might be obscured AGNs.

With these motivations in mind, we have selected a well-studied, strong-lensing galaxy cluster field, SMACS 0723 (Medezinski et al. 2007; Ebeling et al. 2010; Repp & Ebeling 2018) to carry out an analysis of the uses of MIRI data for uncovering galaxy properties. Previous research on this cluster field has been conducted using various telescopes and instruments, including *Chandra, VLT/MUSE, Subaru*, the *Hubble Space Telescope* (Reionization Lensing Cluster

Downloaded from https://academic.oup.com/mnras/article/531/1/617/7675333 by Liverpool John Moores University user on 23 September 2024

Survey; Coe et al. 2019), and *Planck* (e.g. Richard et al. 2021; Golubchik et al. 2022; Lagattuta et al. 2022; Mahler et al. 2023). Mahler et al. (2023) determined the cluster redshift to be $z = 0.3877$ based on a sample of 26 spectroscopically confirmed cluster members. They also derived a cluster velocity dispersion of $\sigma \sim 1180 \pm 160$ km s^{-1}. According to the Planck estimation, the total mass of the cluster is approximately $8.39 \times 10^{14}\,M_{\odot}$ (Coe et al. 2019). Previous infrared observations with the *Spitzer* and *Herschel* Space Telescopes have revealed the presence of a population of dusty, infrared-luminous, red-sequence galaxies in the SMACS0723 field (Sun et al. 2021, 2022).

In this paper, we use JWST MIRI observations of SMACS0723 to study the role of MIRI in measuring photometric redshifts of distant galaxies and to study the physical properties of the potentially dusty and AGN galaxies which are obscured at optical bands. This is important as we know that the fraction and amount of AGN at high-z is perhaps surprisingly high (e.g. Juodžbalis et al. 2023). Thus it is important to determine how we can measure the amount of AGN and their contribution to galaxy SEDs. Thus, this paper focuses on the selection and analysis of dusty galaxies selected by MIRI bands in conjunction with HST and JWST/NIRCam data.

The structure of the paper is organized as follows. We describe the JWST and the ancillary data sets used in this study and the data reduction process in Section 2. We also describe the catalogue generation process. In Section 3, we present the MIRI selected sample and the physical properties from the SED fitting for the galaxy. In Section 4, our study focuses on the notable advancements achieved through the utilization of MIRI data. We examine the enhancements it brings to various aspects, such as the accuracy of redshift measurements, the characterization of star populations in galaxies, and the impact on the SED analysis of both active galactic nuclei (AGNs) and SFGs. In Section 5, we provide a summary of our findings and discuss the potential avenues for future research in this field.

Throughout this paper, we assume a flat cosmological model with $\Omega_{\Lambda} = 0.7$, $\Omega_m = 0.3$ and $H_0 = 70 \mathrm{km\,s^{-1}\,Mpc^{-1}}$. All magnitudes used in this paper are in the AB system (Oke & Gunn 1983).

2 DATA REDUCTIONS AND CATALOGUE

2.1 JWST NIRCam observations

Observations of the SMACS-0723 galaxy cluster were taken on 2022 June 06, as part of the Early Release Observations (ERO) programme (ID: 2736, PI: K. Pontoppidan, Pontoppidan et al. 2022). The observations consist of 6 NIRCam photometric bands F090W, F150W, F200W, F277W, F356W, and F444W. The total integration time is 12.5 h. Our NIRCam image reduction is performed using the procedure of Ferreira et al. (2022) and Adams et al. (2023). Below we summarize the procedure. The data were processed using the JWST Calibration Pipeline (v1.8.2 and CRDS v0995) using the default parameters for stages 1 and 2. This was the most up-to-date version at the time of writing, and includes the second round of post-flight calibrations. We then apply the 1/f noise correction[1] derived by Chris Willott after stage 2. After stage 3, we subtract an initial flat background and carry out a 2-dimensional background subtraction. Then we align the final F444W image onto a GAIA-derived WCS using `tweakreg`, as part of the DrizzlePac python package. We then match all remaining filters to this derived F444W WCS.[2] We then pixel-match the images to the F444W image with the use of `astropy reproject`.[3] The final resolution of the drizzled images is 0.03 arcsec pixel^{-1}.

We use the `SExtractor` (Bertin & Arnouts 1996) version 2.8.6 to identify our sources. We run this in dual-image mode with the F444W image used for object selection. Here the apertures of all measurements should be consistent. MIRI's PSF FWHM is 0.5 arcsec in the F1500W filter. Thus we conduct forced circular aperture photometry within 1.0 arcsec diameters. We perform the aperture correction derived from simulated `WebbPSF` point spread functions[4] for each NIRCam band. We experimented with many different aperture photometry measurement methods and found that this one is the best for recovering accurately the fluxes of our galaxies. The effects of galactic extinction are negligible in these IR bands (<0.1 mag), and thus are not applied.

2.2 JWST MIRI observations

MIRI observations for this field were taken on 2022 June 14, covering a specific area measuring 112″.6 × 73″.5. The data acquisition included observations in the F770W, F1000W, F1500W, and F1800W bands within this field. In the first version of this analysis, we use the data processed from the `grizli` reduced by Brammer et al. in prep.[5] The data were processed using CRDS v0995 calibration file. The cosmic rays and detector-level corrections, including linearity, dark current, and jump detection have been corrected. After that, we performed 2-dimensional background subtraction using `photutils` (Bradley et al. 2022), ensuring that the background has been properly subtracted. The resulting drizzled images have a resolution of 0.04 arcsec pixel^{-1}. And the 5σ depth at F770W is 24.95 AB mag.

In September 2023, the MIRI Team has delivered significant updates[6] to the Imaging and Coronagraphic Imaging flux calibration reference files. To validate the issues related to MIRI flux calibration and assess their potential impact on SED analysis results, we re-reduced the data using the JWST standard pipeline with the new calibration file CRDS v1148 using the default parameters in stage 1 and 2. We correct the cosmic rays and detector noise. We run the default step to subtract the background. However, the reduced images reveal the presence of pronounced background patterns, specifically stripes and gradients, pre-dominantly around the edges of the images. The central region of the image exhibits no discernible impact from these artefacts. Thus, we conducted a custom image processing to address the stripe issues. Briefly, we subtract locally along both rows and columns (subtracting the median) after masking the regions around bright sources. Here, we choose 10 × 10 pixels in each box. The overall effect of reducing the stripes is significant. A similar process is carried on in relevant MIRI papers, e.g. Álvarez-Márquez et al. (2023), Lyu et al. (2023).

Comparing the results with the previous calibration file CRDS v0995, the magnitude deviations for MIRI bands are as follows: Δm[F770W, F1000W, F1500W, and F1800W] = [0.17, 0.05, 0.03, and 0.05]mag. These values are derived by calculating the median of

[1] https://github.com/chriswillott/jwst

[2] https://github.com/spacetelescope/drizzlepac

[3] https://reproject.readthedocs.io/en/stable/

[4] https://jwst-docs.stsci.edu/jwst-near-infrared-camera/nircam-performance/nircam-point-spread-functions

[5] Images and catalogs of JWST/MIRI in the SMACS0723 field processed with the `grizli` software pipeline: https://zenodo.org/record/6874301

[6] https://www.stsci.edu/contents/news/jwst/2023/updates-to-the-miri-imager-flux-calibration-reference-files

Downloaded from https://academic.oup.com/mnras/article/531/1/617/7675333 by Liverpool John Moores University user on 23 September 2024

Δ_m for bright sources with $m < 22$ mag. In the F770W band, $\Delta m_{\rm F770W} = 0.17$ mag implies an average flux reduction of approximately 15 per cent. In comparison to local depth, the deviations fall within the error range (local depth), except for the F770W band. Therefore, the impact on other bands is negligible, with the only noteworthy consideration being the F770W band. Therefore, we applied an additional correction factor of $\Delta m_{\rm F770W} = 0.17$ mag to the data for F770W. We find the results of the SED fitting do not change much with this.

We then align the images to NIRCam F444W matching systems with separations $\Delta < 0.05$ arcsec. We then we run `SExtractor` version 2.8.6 (Bertin & Arnouts 1996) in dual-image mode to detect objects in each field. The detection image we use is MIRI F770W. We use the F770W filter as it has the best sensitivity and angular resolution in the MIRI bands. The apertures of 1.0 arcsec are the same as before. We also perform aperture corrections derived from simulated `WebbPSF` MIRI point-spread functions[7] for each band. The observed MIRI PSFs at $< 10\,\mu$m exhibit cruciform artifacts caused by internal reflections in the camera, that the simulated WebbPSF models do not include. It mostly affects the F560W and F770W bands. We plot the enclosed flux vs radius of Gaia stars in the field and compare it to the WebbPSF. It suggests its influence <5 per cent at F770W, covered by our 10 per cent min errors. The aperture corrections are essential as it allows us to measure photometry on different bands and then to normalize these measurements by correcting for the effects of using an aperture which by its nature limits the amount of flux measured.

2.3 HST imaging observations

HST observations of SMACS0723 are from the Reionization Lensing Cluster Survey (RELICS). This survey observed 41 massive galaxy clusters with Hubble and Spitzer at 0.4–1.7 μm and 3.0–5.0 μm, respectively. SMACS0723 (ID: GO 14017; Coe et al. 2019) was observed in one WFC3/IR pointing, with a total of 10 orbits in WCS3/IR (F105W, F125W, F140W, and F160W) and ACS imaging (F435W, F606W, and F814W). The observational details and the HST data reduction are available from Coe et al. (2019). The image resolution is 0.06 arcsec pixel^{-1}.

As mentioned before, before the source extraction we align the HST images to NIRCam F444W to a level of $\Delta < 0.05$ arcsec. Then we run `SExtractor` version 2.8.6 (Bertin & Arnouts 1996) in dual-image mode to detect objects in the field with an aperture of 1.0 arcsec for photometry measured in each filter image. The weighted stack of all the HST images is the input detection image, the same as that in Coe et al. (2019).

We also perform aperture corrections based on the ACS/WFC[8] and WFC3/IR PSF[9] encircled energy fraction. We correct all photometry for Galactic extinction using the IR dust emission maps of Schlafly & Finkbeiner (2011).

2.4 Source photometry and cataloguing

To generate a matched catalogue for all the sources in SMACS0723, we use `TOPCAT` to combine SExtractor's HST and JWST catalogs. The maximum separation allowed is 0.3 arcsec, which is a good compromise between the false-positive rate achieved and how restricted it is due to the size of MIRI's PSF. For the final catalogue, we use a forced circular 1 arcsec diameter aperture. This diameter is chosen to enclose the central/brightest ∼86 per cent of the flux of a point source of NIRCam and ∼83 per cent of MIRI, enabling us to use the highest SNR pixels to calculate galaxy colours while avoiding reliance on strong aperture corrections that can be as high as the actual measurements made. It is also consistent with the circular apertures of 0.9 arcsec diameter in Papovich et al. (2023). Additionally, we create a composite mask to avoid image artefacts. These masks cover diffraction spikes, the few remaining snowballs in the NIRCam imaging, as well as regions of intra-cluster medium (in the NIRCam modules containing any foreground cluster), and a buffer around the edges of the observations. The remaining total unmasked region is ∼2.3 arcmin^2. We plot the NIRCam and MIRI observations overlaid on the HST ACS F606W image, in Fig. 2.

When computing the stellar mass and SFR for individual galaxies, we generate SEDs using aperture-corrected photometry with the same aperture size, that might underestimate the total flux for resolved sources. To address this, we apply a simple correction factor based on the ratio between the aperture and total photometry (`MAG_AUTO`) measured by `SExtractor` in the F444W band. The relevant physical parameters, SFR and stellar mass, have been corrected.

`SExtractor` is known to underestimate the photometric errors of sources. To ensure accurate measurements, we calculate the local depth of our final images. We place circular apertures (1 arcsec) in empty regions that are about 1 arcsec away from real sources in our images. We use the measured background flux in these apertures to derive a median depth for each field. Finally, we calculate the photometric errors for each individual source using the nearest 200 empty apertures to determine the local depth. The 5σ depths of each band can be found in Table 1.

Finally, we use robust methods to construct the final samples. The relevant selection criteria are described in Section 3.2. In total, 181 galaxies are matched and meet our selection criteria. To comprehensively detect all sources in this field, especially at high redshift, we use NIRCam as the detection image and strive to determine the corresponding measurements for HST and MIRI. Specifically, we use `SExtractor+ +` (Bertin et al. 2022) in dual-image mode to measure HST and MIRI fluxes for the NIRCam detections. For high-redshift galaxies at $z > 6.5$, their blue-ward bands (HST) are anticipated to appear faint or undetected due to the Lyman break. Out of the total of 12 candidates at $z > 6.5$ identified by NIRCam, unfortunately, these candidates are not within the coverage of MIRI and HST. More detailed analysis of this $z > 6.5$ sample can be found in our EPOCHS paper I (Conselice, in preparation).

SMACS0723 is a strong-lensing field, we correct the lensing effect on all galaxies situated behind the galaxy cluster to extract the physical properties of these galaxies, e.g. stellar mass and SFR. We employ a lens model from RELICS, that is computed using `Lenstool` (Sharon et al. 2023). Then, we excluded sources near the center of the cluster ($\mu > 5$) to mitigate issues related to multiple imaging and excessive gravitational amplification. All the physical properties of these galaxies in this paper have been corrected for the effects of lensing.

Considering the wavelength-dependent morphology of galaxies that may lead to chromatic effects, we have chosen galaxies with the highest μ/magnification ($\mu \sim 5$) to investigate potential differences in their SEDs when using APER magnitude

[7] https://jwst-docs.stsci.edu/jwst-mid-infrared-instrument/miri-performance/miri-point-spread-functions
[8] https://www.stsci.edu/hst/instrumentation/acs/data-analysis/aperture-corrections
[9] https://www.stsci.edu/hst/instrumentation/wfc3/data-analysis/photometric-calibration/ir-encircled-energy

Downloaded from https://academic.oup.com/mnras/article/531/1/617/7675333 by Liverpool John Moores University user on 23 September 2024

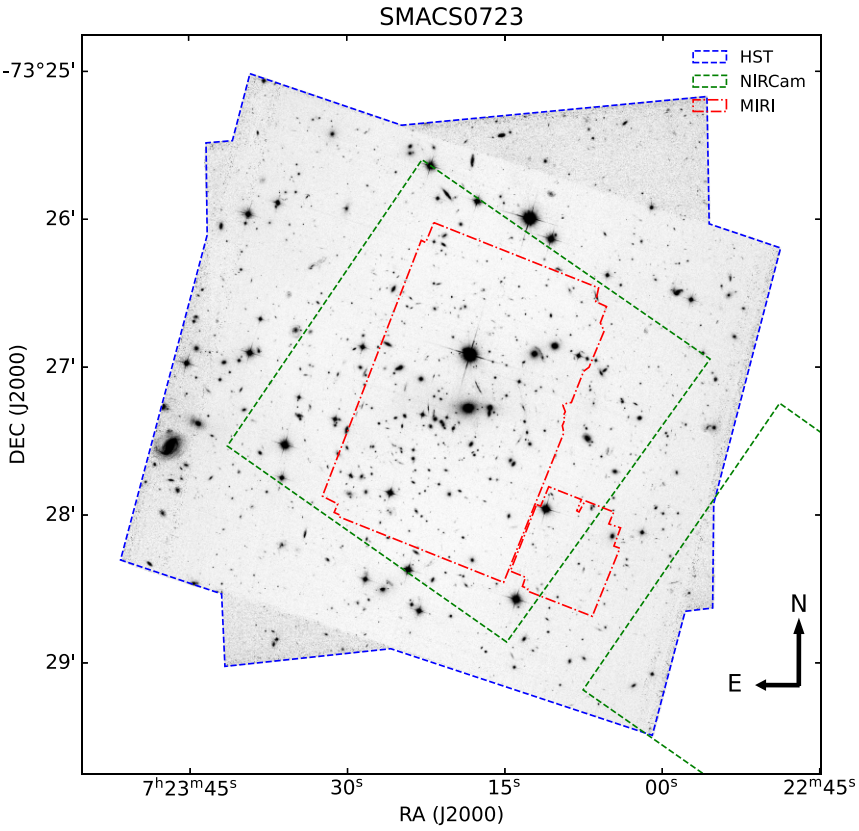

Figure 2. The SMACS0723 fields of view overlaid on HST images (R:JWST/MIRI, G:JWST/NIRCam, B:HST). Before generating the catalog, we produce a mask to avoid the diffraction spikes of bright stars and image artifacts. These masks cover diffraction spikes, the few remaining snowballs, regions of intra-cluster medium, and a buffer around the edges of the images. The imaging data is from HST, the green dotted boxes show the coverage of NIRCam, and the red dashed lines show the area imaged by MIRI.

Table 1. 5σ depths and correction factors of magnitude-zeropoints, apertures and extinctions.

Instrument/Filter (1)	Zeropoint AB mag (2)	Aperture correction AB mag (3)	5σ depths AB mag (4)
HST/F435W	25.66	−0.106	25.14
HST/F606W	26.50	−0.095	25.39
HST/F814W	25.95	−0.098	25.23
HST/F105W	26.27	−0.136	25.17
HST/F125W	26.23	−0.155	24.87
HST/F140W	26.45	−0.164	24.67
HST/F160W	25.95	−0.170	25.19
NIRCam/F090W	28.08	−0.079	27.08
NIRCam/F150W	28.08	−0.090	26.91
NIRCam/F200W	28.08	−0.103	26.99
NIRCam/F277W	28.08	−0.110	27.40
NIRCam/F356W	28.08	−0.119	27.57
NIRCam/F444W	28.08	−0.143	27.43
MIRI/F770W	28.9	−0.202	24.95
MIRI/F1000W	28.9	−0.326	25.15
MIRI/F1500W	28.9	−0.369	24.65
MIRI/F1800W	28.9	−0.421	24.18

(aperture-corrected) compared to AUTO magnitude. The colour difference ($\Delta_{\rm color} = {\rm color}_{\rm APER} - {\rm color}_{\rm AUTO}$) for F277W-F1000W is −0.04 mag, which is negligible in comparison to the magnitude errors.

3 MIRI SELECTED GALAXIES

In the following sections, we describe the main results of this paper. We outline SED fittings with and without MIRI, using `cigale` and `EAZY` and identify the types of galaxies that are preferentially selected with MIRI included to the depths we are reaching. Additionally, we will explore whether MIRI is capable of observing more galaxies compared to using NIRCame alone.

3.1 Spectral energy distribution modelling

After generating our catalogues, we fit the SEDs of each source to derive photometric redshifts in various different ways. To calculate a preliminary photo-z, we fit SEDs using `cigale` (Boquien et al. 2019). `cigale` better constrains the fluxes on the redder bands because it includes AGN contributions and more accurate dust templates compared to `EAZY`, which we use in other EPOCHS papers (e.g. Adams et al. 2023). Here, we follow the setups used by Yang et al. (2023).

We use the standard delayed-τ 'sfhdelayed' star formation history within our fitting. We set the e-folding time and stellar age to vary from 0.5–5 and 1–5 Gyr, respectively. We use Bruzual & Charlot (2003)(BC03) templates for the stellar population (SSP) models, assuming a Chabrier (2003) initial mass function (IMF), with a solar metallicity of $Z = 0.02$. We also include within our fits the nebular module (Villa-Vélez et al. 2021) for emission from the HII regions,

Downloaded from https://academic.oup.com/mnras/article/531/1/617/7675333 by Liverpool John Moores University user on 23 September 2024

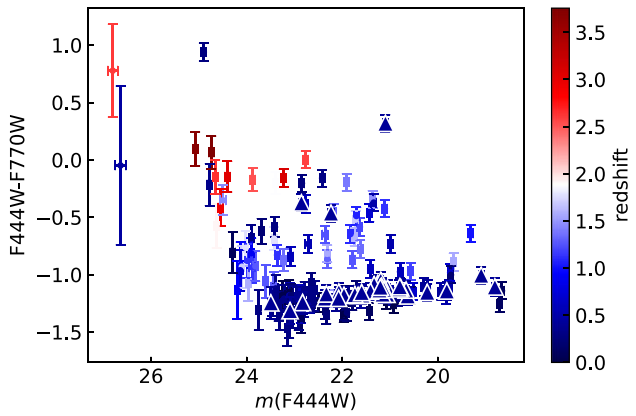

Figure 3. Plot of observed NIRCam and MIRI mag-colour diagram for the matched robust galaxies in SMACS0723 field. The magnitude error is calculated using measurements of the local depth. The redder colour corresponds to higher redshift galaxies. A gradient in redshift can clearly be seen in the F444W-F770W colour. Quiescent galaxies in the cluster are represented by triangles.

with an ionization parameter of $\log U = -2.0$, a gas metallicity $= 0.02$ and with lines width $= 300.0$ km s^{-1}.

We use the 'skirtor2016' module to describe the AGN component (Stalevski et al. 2012, 2016), with the fraction of AGN $\texttt{frac}_{\rm AGN}$ varying from 0 to 0.99 and the relative rest-frame wavelength $\lambda_{\rm AGN}$ in the range of 3–30 μm. The 9.7 μm optical depths allowed in our study includes all available values 3, 5, 7, 9, and 11. We fix the AGN viewing angle to be at 70 degrees to select the obscured AGN, which is a typical value for type II AGN (Yang et al. 2020, 2022).

We also use the 'dl2014' module developed by Draine et al. (2014) to calculate dust emission. The dust emission comprises two components: a diffused emission and a photodissociation region (PDR) emission associated with star formation. In our fitting, we allow the fraction of PDR emission (γ) to vary from 0.01 to 0.9, the minimum radiation parameter (Umin) to vary from 0.1, 1.0, 10, 50, and a maximum fixed value of Umax $= 10^7$. The mass fraction of PAH in total dust is the same for both components, and we set it as [0.47, 2.5, 7.32]. For the dust attenuation, we adopt the 'dustatt' modified starburst module in `cigale` (Calzetti et al. 2000; Leitherer et al. 2002). The colour excess is set within the range $E(B-V) =$ 0–1.

In order to determine the most accurate photometric redshifts, we use the redshifting mode and a redshift grid ranging from $z =$ 0.0 to 15.0, with a bin width of 0.1. We measure the properties of our sample of galaxies, including redshift, SFR, stellar mass, and $\texttt{frac}_{\rm AGN}$ through both traditional least-$\chi 2$ analysis and different types of Bayesian approaches. The latter methods take into account the full probability density functions, and provides more comprehensive and informative results than the least-χ^2 approach (Boquien et al. 2019).

In addition, we also utilize the `EAZY` photometric redshift code (Brammer, van Dokkum & Coppi 2008) to assess the accuracy of the SED fitting derived from `cigale`, and `EAZY`, in conjunction with HST and NIRCam data. Our `EAZY` approach involves a modified Kroupa IMF (Kroupa 2001) and the default templates (tweak_fsps_QSF_12_v3), which is comprised of younger stellar populations, lower metallicities, and more active star formation (Larson et al. 2023).

The comparison between the redshift measurements obtained from these methods reveals a high level of concordance, with deviations typically falling within 15 per cent, except for a small subset of targets (8/181) fit using `EAZY` at a redshift of approximately $z \sim 6$. Due to the the limited availability of dust and AGN templates at the red wavelengths, `EAZY` exhibits a less restrictive approach towards the data. It tends to primarily rely on the blue end of the data, using Lyman-break or Balmer-break techniques for redshift determination. This inclination can result in potential contamination when selecting samples with high redshifts at $z > 6$. It is important to note that the occurrence of such sources is relatively scarce. Therefore, when publishing high-redshift candidates, additional stringent selection criteria need to be employed for accurate screening, a topic which is discussed in our EPOCHS paper I (Conselice, in preparation). Nevertheless, our results provide strong evidence supporting the reliability and stability of our SED fitting technique when leveraging the rich photometric information provided by HST and NIRCam observations. None the less, an important conclusion from our study is that some low redshift galaxies can be mistaken for high redshift ones without the use of MIRI data.

3.2 A robust sample of MIRI selected galaxies

In order to determine the physical properties of MIRI selected galaxies, we utilize the `cigale` SED fitting approach outlined in Section 3.1. We employ a series of selection criteria described below:

(i) We require detections in both MIRI and NIRCam: $\geq 5\sigma$ detection in 2 bands in MIRI, and $\geq 5\sigma$ detections in 2 bands in NIRCam.

(ii) Removal of the sources close to the centre of the cluster to avoid multiple imaging and excessive gravitational amplification caused by lensing.

(iii) Morphology checking to exclude non-galaxy targets, e.g. hot pixels, artefacts, blended features.

(iv) Matching with HST catalogue within 0.3 arcsec; for non-matched targets, we use `SExtractor+` + with the forced aperture to collect the flux at its position.

(v) We require $\chi^2_{red} < 6$ for best-fitting SEDs to be classed as robust.

(vi) $P(z_{sec}) < 0.5 \times P(z_{phot})$ to ensure the probability of a secondary peak, if one exists, is less than 50 per cent of the high-z solution.

The broad emission features of PAHs in the 3–20 μm range are shifted to longer wavelengths with increasingly higher redshifts. As a result, these features are expected to dominate the flux at specific mid-infrared wavelengths, leading to significant redshift-dependent colour variations in broad-band photometry (Langeroodi & Hjorth 2023). In Fig. 3, we present the NIRCam and MIRI magnitude-colour (F444W versus F444W-F770W) diagram for our sources, while the colour-colour (F444W-F770W versus F770W-F1000W) diagram is shown in Fig. 4.

As explained earlier, we determine redshifts using a Bayesian analysis based on `cigale` fitting. In Fig. 3, we observe a considerable number of cluster members that do not exhibit PAH emission and have low specific star formation rates (sSFR). Their redshifts are around $z = 0.4$ and they are located at the bottom of the mag-colour plot. In Fig. 4, we find that galaxies primarily occupy the region towards the bottom left of the colour-colour diagrams, in several magnitudes of the flat-spectrum point located at position (0,0). Due to their colours, this region is likely populated by quiescent galaxies and higher redshift galaxies.

Downloaded from https://academic.oup.com/mnras/article/531/1/617/7675333 by Liverpool John Moores University user on 23 September 2024

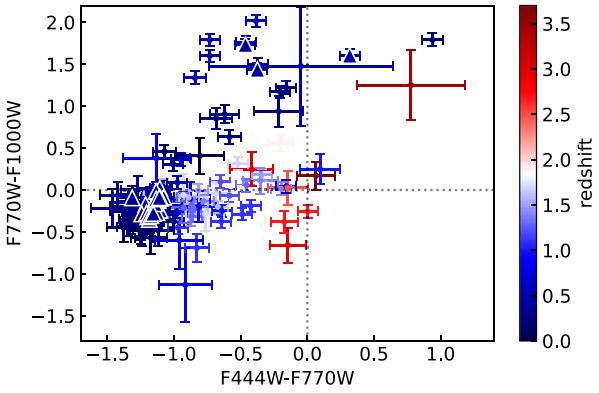

Figure 4. Colour-colour diagram of NIRCam and MIRI bands for the matched galaxies in SMACS0723. The symbols and points are otherwise the same as in Fig. 3.

We group our sources into the following primary categories based on the criteria above and primarily from the χ^2_{red} fits. Figs 5 and 6 summarize the cutout images and SED fitting results for each category.

(i) AGN: The emission from AGN in the MIRI bands can arise from several components. One component is the thermal emission from the dusty torus surrounding the central black hole (Fritz, Franceschini & Hatziminaoglou 2006; Nenkova et al. 2008; Siebenmorgen, Heymann & Efstathiou 2015) The temperature of the torus typically ranges from a few hundred to several thousand degree K, depending on the AGN's level of activity. This emission is influenced by the temperature and geometry of the torus, as well as the orientation of the system with respect to the observer. Another contribution from AGN at the MIRI bands is non-thermal emission originating from relativistic jets or outflows associated with the black hole (e.g. Kotilainen et al. 1992; Neugebauer & Matthews 1999). These high-energy particles can produce synchrotron emission in the mid-infrared regime, which can be detected by MIRI. Disentangling the AGN contribution from other sources, such as star formation, allows for a more comprehensive analysis of the galaxy's overall emission and underlying processes. We will discuss this in more detail in Section 4.3.

(ii) High-z galaxies: With the broad wavelength coverage of the MIRI bands on JWST, several techniques can be employed to select $z > 2$ galaxies. Flux dropouts or steep declines in the SED due to Lyman and Balmer breaks can be identified as indicators of high-redshift sources. Additionally, MIRI enables the detection of key emission features, such as PAH, which are redshifted to longer wavelengths for high-redshift sources, making them accessible in the MIRI bands. At the most elevated redshifts ($z > 10$), MIRI is the sole instrument capable of offering a groundbreaking opportunity to observe robust optical emission lines ([O III] 4959,5007Å, H_α, H_β). Leveraging the IR capabilities of JWST, we successfully applied the Lyman and Balmer break to select high-z objects that may be undetectable or faint in blue bands like HST and F115W. MIRI photometry provides robust constraints on the SEDs, enabling precise determinations of redshift and galaxy properties. In our final catalog, we identified 46 galaxies at $z_{\rm photo} > 1$, of which 29 (63 per cent) have confirmed high spectroscopic-z values (Caminha et al. 2022; Carnall et al. 2023; Noirot et al. 2023). For a detailed description of our study on high-z objects at $z > 6.5$, see our EPOCHS paper I (Conselice, in preparation).

(iii) Dusty star-forming galaxies: MIRI offers a range of methods to search for dusty SFGs. The thermal emission from dust heated by UV/optical photons from young, massive stars can be detected using the MIRI bands. Moreover, The presence of PAH features at 6.2, 7.7, 8.6, 11.3, and 12.7 μm indicates actively SFGs, especially at high redshift (e.g. Langeroodi & Hjorth 2023). Additionally, MIRI's broad wavelength coverage allows us to measure the SED shape and identifying characteristic features, such as the 9.7 μm silicate feature (Rich et al. 2023), to investigate whether the galaxy is obscured in the mid-IR. We employ the 'dl2014' module in `cigale`, which is comprised of a diffused emission and a PDR emission associated with star formation and PAH features. This fully considers the above situation and can effectively select dusty SFGs.

(iv) Quiescent galaxies: Quiescent galaxies are characterized by a low level of ongoing star formation and are typically associated with an older stellar population. In the colour-colour diagram shown in Fig. 4, some quiescent galaxies tend to be found within a cluster at a redshift of $z_{cl} = 0.39$ and are observed to have a colour of (F770W–F1000W) ~ -0.5 mag (AB), which is consistent with the predictions of the quiescent galaxies models (fig. 1 of Langeroodi & Hjorth 2023). Quiescent galaxies tend to cluster in the region towards the bottom-left of the stationary locus of the star-forming tracks. The position of these quiescent galaxies in this region are roughly independent of redshift due to their approximately power-law SEDs. We identified all the cluster galaxies occupying the region corresponding to quiescent galaxies using spectroscopic redshifts from MUSE observations ($z = 0.387 \pm 0.02$) as reported in Caminha et al. (2022). This is expected as various quenching mechanisms operate more efficiently in cluster environments (e.g. Donnari et al. 2021; Kim et al. 2023). Furthermore, in addition to the quiescent sources within the cluster, several quiescent galaxies at redshifts around $z \sim 1$–2 have been discovered within overdensities associated with a significant number of SFGs (e.g. Noirot et al. 2023).

We also check for sources with only MIRI detections, that are not found within NIRCam or HST observations. To ensure that we do not miss these sources, we utilised `SExtractor+ +` and searched for detections with a 5σ threshold or higher on at least two MIRI bands. We then measure the NIRCam and HST flux at the same positions as before, using the same aperture and mask. Interestingly, we did not find any sources that are only detected solely with MIRI, indicating that NIRCam photometry is deep enough within this field and at the MIRI depth we study to capture all the IR bright sources. The 5σ depth of F770W and F1000W is 24.95 and 25.15 mag, which is 3 mag shallower than NIRCam F444W of 27.43 mag. This suggests that previous JWST work that relied solely on NIRCam detections is reliable in finding all galaxies to our MIRI depth.

4 STARS, DUST, AND AGN PROPERTIES

In this section we discuss the physical properties of our MIRI selected galaxies. We first explore their redshift, stellar mass and star formation history derived by `cigale` fitting and then we investigate how MIRI can improve the accuracy of these measurements. Additionally, we also analyse the AGN contribution and conduct a detailed study of the median SED of the selected galaxies.

4.1 The impact of MIRI on redshift measurement

Limited by the available JWST observations, most recent photo-z redshift measurement works only focus on the NIRCam analysis (e.g. Adams et al. 2023; Bouwens et al. 2023; Endsley et al. 2023). Here we test how and if MIRI improves the accuracy of photo-z redshift mea-

Downloaded from https://academic.oup.com/mnras/article/531/1/617/7675333 by Liverpool John Moores University user on 23 September 2024

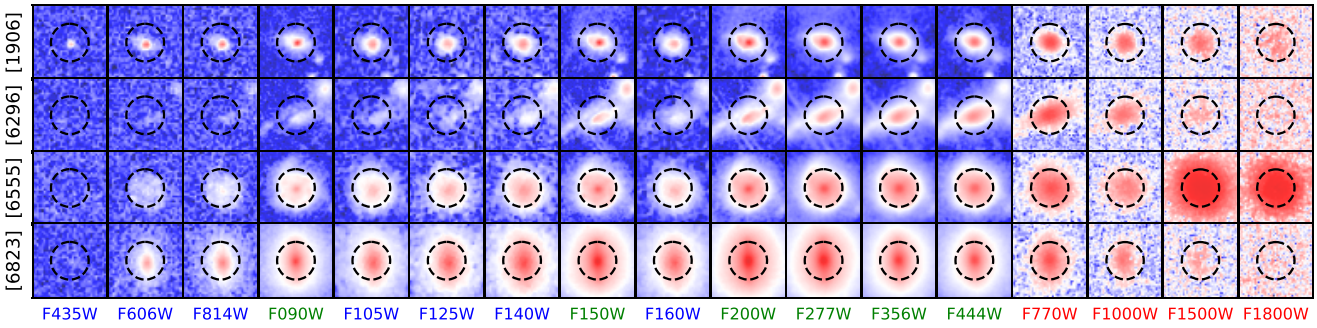

Figure 5. The different band images of a subset of the galaxies in log scale. Their IDs are labelled on the left. From left to right, the images are ACS F435W, ACS F606W, ACS F814W, NIRCam F090W, WCS3 F105W, WCS3 F125W, WCS3 F140W, NIRCam F150W, WCS3 F160W, NIRCam F200W, NIRCam F277W, NIRCam F356W, NIRCam F444W, MIRI F770W, MIRI F1000W, MIRI F1500W, and MIRI F1800W. The text in blue, green, and red denotes different instruments: HST, NIRCam, and MIRI, respectively. The images are 2×2 arcsec^2 and are centred on the galaxy in each bandpass. The black circle is the aperture of 1 arcsec.

surements. We use the `cigale` code again to determine the photo-z redshift with and without MIRI data. The parameters in the fit are the same as before. The results show that the photo-z redshifts are nearly consistent, as shown in Fig. 7. These two methods have photometric redshift solutions within 15 per cent of that with MIRI. In addition, we find `cigale` fitting with MIRI data decreases the uncertainty of photo-z redshifts $(\sigma_{\rm MIRI} - \sigma_{\rm noMIRI})/\sigma_{\rm MIRI}$ by 50 per cent.

In Fig. 7, there are three objects that stand out as outliers with a difference greater than $\Delta z > 2$. When using MIRI to measure photometric redshifts, these objects are at high redshifts $z_{phot} > 2.5$, whereas without MIRI, the derived redshift is $z < 1.0$. The identification of good photometric redshifts relies on either the Lyman break or Balmer break. While fitting without MIRI data, the photo-z code fits the gap between HST/ACS F435W and F606W as the Balmer break, thereby identifying them as being low redshift. However, fitting with MIRI data could change the measurement of photo-z redshift in two aspects. First, MIRI data could improve constraints on the dust emission/attenuation at the redwards wavelength. Secondly, another factor to consider is the impact of nebular emission lines, including the PAH feature, on the flux in certain bands. This can potentially cause significant changes in the photometric redshift solutions. In such cases, the code fits the observed NIRCam/F200W excess as a Balmer break, resulting in a high-z solution.

Although there are currently 17 multiband data points available in this field that effectively and accurately distinguish between high-z and low-z targets, it is evident that relying solely on photometry still creates significant uncertainties. Currently, 85 (∼50 per cent) of our galaxies have spectroscopic redshift information available. In Fig. 8, we present a comparison between the spectroscopic redshift and the photometric redshift with and without MIRI. The spectroscopic redshifts are measured by Suburu, VLT/MUSE, JWST/NIRISS and JWST/NIRSpec(Caminha et al. 2022; Carnall et al. 2023; Noirot et al. 2023). The photometric redshift data are almost all located within 15 per cent of the spectroscopic redshift. It can be seen that the photometric redshift is quite reliable to a certain extent, even when utilising only HST and NIRCam data. This is due to the fact that the Lyman break/Balmer break is the basis for the photometric redshift, which relies more heavily on data from the blue end. In contrast, an absence of HST data can cause a significant bias in the photometric redshift.

Fig. 8 (right) displays the relative difference between the spectral redshifts and photometric redshifts with and without MIRI data. This reveals that median photometric redshift estimates have a scatter of $0.00^{+0.01}_{-0.05}$ (0.1 per cent) and $-0.04^{+0.04}_{-0.03}$ (4.0 per cent) from the spectroscopic redshift for fits with and without MIRI data, respectively. The outlier fractions, defined as the fraction of photometric redshift that disagrees with the spectroscopic redshift by more than 15 per cent in $(1 + x)$, $(|\Delta z|/(1 + \text{spec-}z) > 0.15)$, are 1 per cent and 5 per cent, respectively. Additionally, the results obtained from fitting with MIRI data show a closer alignment with the spectroscopic redshift and reduce the estimated errors on the photometric redshift by $(\sigma_{\rm X} - \sigma_{\rm spec})/\sigma_{\rm spec}$ of 20 per cent.

At present, spectroscopic observations are mostly at low redshifts. In the SMACS0723 field, only 10 sources with a redshift greater than 6.5 have been observed by NIRCam, and unfortunately, they have not been covered by MIRI observations. JWST mid-infrared and spectroscopic observations are still lacking at this stage. Upcoming follow-up studies are expected to provide more data, which will help to systematically constrain their redshifts and physical properties.

4.2 Stellar mass and star formation history

Here we discuss the comparisons between star formation rate and masses derived when we include MIRI data and we excluded MIRI data as shown in Fig. 9. We employ the standard delayed-τ 'sfhdelayed' star formation history and the bc03 stellar population module (Bruzual & Charlot 2003), assuming using Chabrier2003 IMF (Chabrier 2003). We have excluded the galaxies from our analysis, which positioned exceptionally close to the cluster's center. We corrected the gravitational amplification for these physical parameters.

In the Fig. 9 (left-hand panel), the majority of stellar mass values fall within a 15 per cent error range. Only a few galaxies lie away from the 1:1 line, but have a large error of >1 dex. The range of preferred values for stellar mass and SFR have been narrowed down with the inclusion of MIRI data. The median $\Delta M_\star$ error decreases 0.1 dex. This is a result of improved constraints on the dust emission and attenuation.

For the star formation rate, `cigale` provides several SFR indicators based on different time-scales: instantaneous SFR, as well as SFRs averaged over the last 10 and 100 Myr. Generally, the SFR averaged over the last 100 Myrs is considered the most reliable indicator of the stable star formation activity. Here we follow this custom to use the SFR averaged over the last 100 Myr. We have excluded the quiescent galaxies with a low star formation rate of $\log \text{sSFR} < -10\,\text{yr}^{-1}$ from this comparison.

Downloaded from https://academic.oup.com/mnras/article/531/1/617/7675333 by Liverpool John Moores University user on 23 September 2024

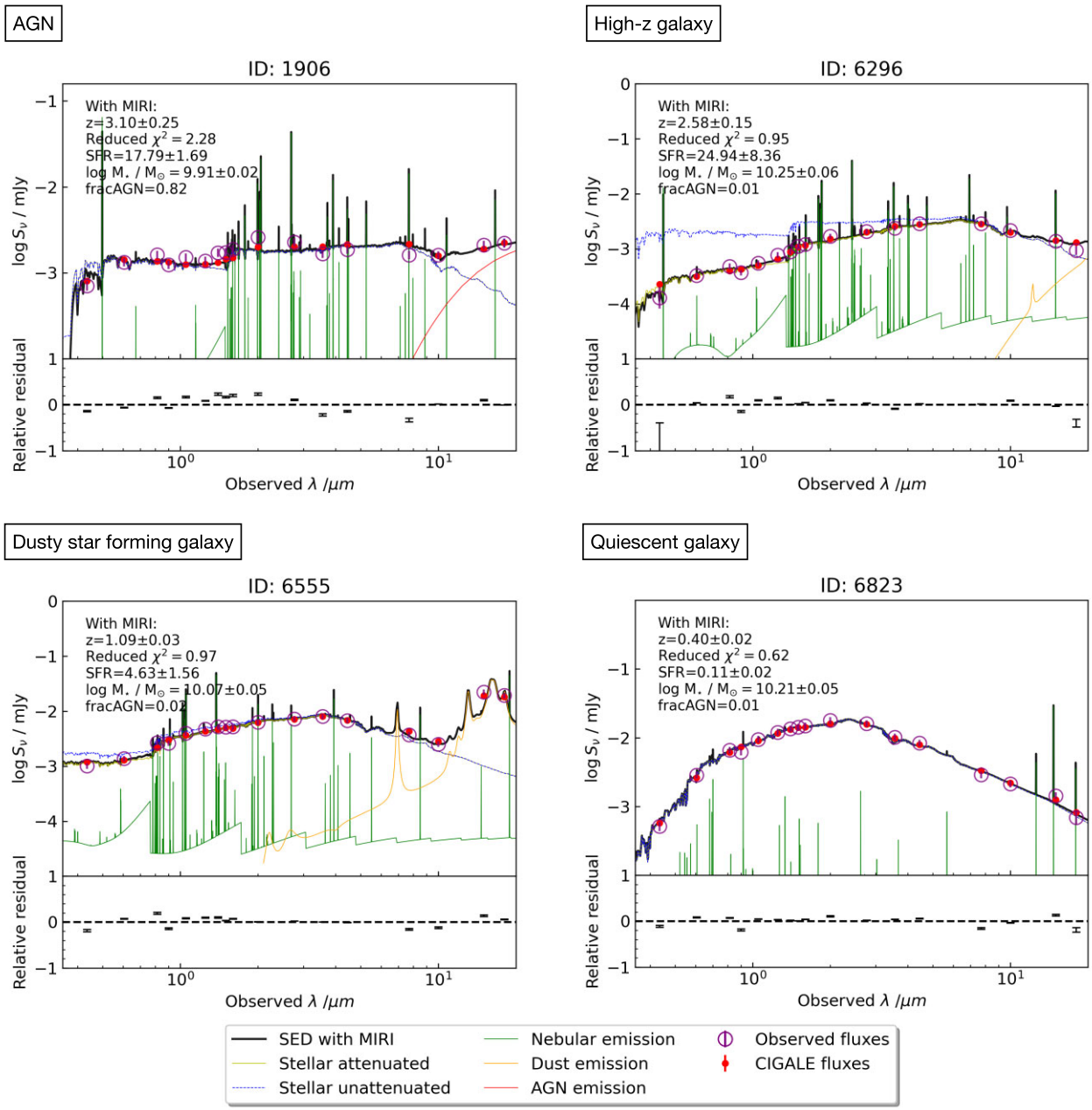

Figure 6. A subset of MIRI selected galaxies with fits done using `cigale` Shown are systems which we classify as AGN, high-z galaxies, dusty star-forming galaxies, and quiescent galaxies. The black line represents the best fitting result from the `cigale` code. The purple points represent the observed fluxes for each band; the red points represent their fitted fluxes. The yellow line represents the star formation contribution; the green line is the fitted emission line template. The red and orange lines represent the contributions of AGN and dust, respectively. The lower part of each panel is the relative residual of the fitting.

The SFRs derived with MIRI data are generally slightly lower by <0.1 dex. Papovich et al. (2023) also reported that adding the MIRI data could reduce SFRs for the galaxies with ΔSFR of 0.15 dex at $4 < z < 6$ and 0.29 dex at $z > 6$, matching our findings. However, for two high-z objects, the log SFRs fitted with MIRI data increase by more than three times, and the error bars also significantly decrease. This is because they are identified as low-z objects with a large uncertainty when we exclude MIRI data. In contrast, adding MIRI changes the best-fitting redshifts, so that they are all $z \sim 3$ objects.

In the middle and right-hand panels of Fig. 9, we re-run the `cigale` fitting with fixed redshift values obtained from fitting with MIRI data. This was done to eliminate the influence of redshift on the results. We can see that the results show good agreement. The results indicate that the impact on the galaxy mass and SFR measurements is primarily a consequence of changing the redshift. This effect can be attributed to the additional information provided by MIRI's mid-infrared observations, allowing for a better constraint on the galaxy's redshift and, consequently, improving the accuracy of its mass and SFR determinations.

Fig. 10 illustrates a representative example of a single galaxy fit, highlighting the significant impact of including MIRI data. The absence of MIRI data results in a loss of constraints at the red-

Downloaded from https://academic.oup.com/mnras/article/531/1/617/7675333 by Liverpool John Moores University user on 23 September 2024

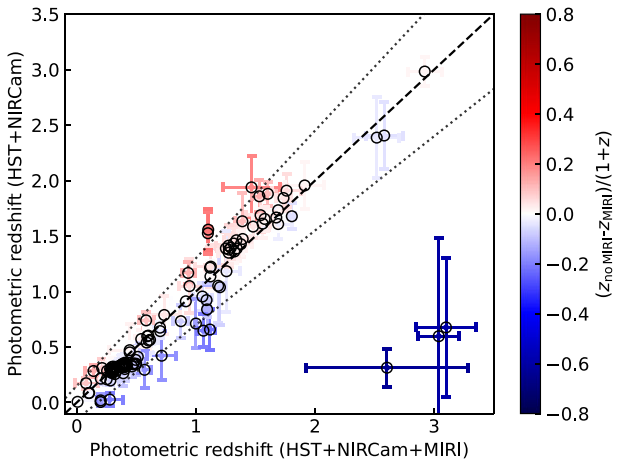

Figure 7. Comparison of the photometric redshifts derived by `cigale` fitting with and without MIRI data. The black dashed line shows the one-to-one relation, which is the ideal 1:1 matching case of photometric versus spectroscopic redshifts. The dotted lines show 15 per cent offsets in $(1 + z)$. The colour of the point represents the relative difference between the photometric redshifts of the galaxies with and without MIRI.

end of the fit, leading to potential inaccuracies in various physical parameters such as redshift determinations. This emphasizes the crucial role of MIRI data in improving the accuracy and reliability of galaxy characterization and analysis.

Generally speaking, including MIRI data gives approximately similar measurements of stellar masses and SFRs to we only using NIRCam and HST. We also find that MIRI reduces the error of the stellar masses and SFRs by ∼0.1 dex, narrowing down the preferred values of stellar population parameters. In some cases, the large differences are always caused by the redshift uncertainties.

4.3 The impact of MIRI on AGN contribution

We measure the contribution of AGN to our sample based on the best-fit $\texttt{frac}_{\rm AGN}$ parameter from `cigale` fitting, and distinguish the galaxies between SFGs and AGNs (referred to as SFG and AGN, respectively). The dale2014 module provides a basic template from the ultraviolet to the infrared for `cigale` fitting. The AGN fraction ($\texttt{frac}_{\rm AGN}$) is defined as the ratio of the AGN luminosity to the sum of the AGN and dust luminosities (Boquien et al. 2019). The dale2014 module is particularly sensitive to data in the red-end at wavelengths of 3 microns to several hundred microns. It covers the emission primarily attributed by the AGN. Thus, we are not using a binary approach to determine if a galaxy is all AGN or all 'stars', but we are determining from this fitting what fraction of the light emitted arises from AGN.

In Fig. 11, we conduct a test to investigate the impact of including or excluding MIRI data on the $\texttt{frac}_{\rm AGN}$ measurement. Our findings indicate that $\texttt{frac}_{\rm AGN}$ has a mean value of 0.09 ± 0.14 in the fit that includes the MIRI data points, which is smaller than the result that does not include MIRI, where we get a fraction of 0.23 ± 0.10. This implies that the MIRI data lower the derived fraction of the AGN and that often the contribution is higher without the use of MIRI. The median $\texttt{frac}_{\rm AGN}$ difference between with MIRI and without MIRI is $-0.15^{+0.09}_{-0.12}$. In Yang et al. (2021), the MIRISIM simulation of CEERS imaging yielded a $\Delta\,\mathrm{frac_{AGN}} = (\mathrm{frac_{AGN,MIRI}} - \mathrm{frac_{AGN,no\,MIRI}})$ value of ∼−0.2 in Fig. 12 Bottom panel, which aligns with our findings of −0.15. In addition, the inclusion of MIRI has caused a significant decrease of ∼0.18 in the error of mean $\texttt{frac}_{\rm AGN}$, similar to the effect on redshift and other galaxy parameters.

However, it becomes challenging to constrain the model in the early Universe, which results in a substantial increase in the error. For instance, at $z < 3$, the warm dust heated by the AGN is well tracked by the MIRI band, with a peak at 10 μm in the rest frame. On the contrary, at $z > 5$, the key emission from AGN-heated dust is shifted beyond MIRI detection ranges. The F1800W band corresponds to the rest frame wavelength of 3 microns, where the contribution of AGN has just started and is still relatively weak. This introduces significant challenges in the pursuit of identifying and investigating AGN beyond a redshift of $z > 3$. We refer readers to see our other paper in this series (Juodžbalis et al. 2023), dedicated to clarifying the complications and strategies entailed in probing AGN at $z \sim 6$.

4.4 SED analysis constraining AGN and dusty contributions

In this section, we analyse the median SEDs of AGN and SFGs using similar redshift ranges and with accurate photometric redshifts. We also investigate the effects of including MIRI data on the median SEDs.

Using $\texttt{frac}_{\rm AGN}$ to identify AGN is not a strict criterion, and the value we use is somewhat arbitrary. To ensure the plausibility of our results, we tested different $\texttt{frac}_{\rm AGN}$ values, ranging from 0.05 to 0.5, to calculate the proportion of AGN to the total number of galaxies, aiming to closely approximate the actual observed results. First, we select 151/181 best-fitting galaxies ($\chi^2 < 6$) and verify to ensure they exhibit a good fit in the red-end of the SED. As a comparison Chiang et al. (2019) used the Northern Ecliptic (NEP) wide-area catalogue who identified 6070 AGNs out of a total of 16 464 IR-selected galaxies. Whilst this catalogue of galaxies is different from the JWST sample as the redshifts and magnitudes of sources are different, as well as having more bands, it does show how to find a reasonable selection for AGN. The fitting for this NEP catalogue used `LePhare` fitting to find AGN. This NEP catalogue consists of 18 mid-infrared filters, including 9 from AKARI, 4 from WISE, and 5 from Spitzer. They found the total proportion of AGN in this NEP catalogue is 36.9 ± 0.5 per cent. Our data set exhibits a comparable redshift distribution within the range of $0 < z < 2.5$, close to that of the NEP sample. Fig. 12 left illustrates our results, we use $\texttt{frac}_{\rm AGN} = 0.1$, that the derived proportion of AGN is most consistent with the NEP observation statistics. In this case, the proportion of AGN (57/151) is 37.7 per cent.

As a result, if an object has a $\texttt{frac}_{\rm AGN}$ value of less than 0.1, we classify it as SFG; otherwise, we classify it as AGN. Using this criterion, we identified 94 SFG and 57 AGN. Fig. 12 right shows the photo-z distributions for different types of objects. We note that slightly altering these empirical classification criteria would not significantly affect our main results.

One way see how different the AGN and star-forming galaxies are in our sample is to compare their SEDs. When generating the median SEDs, we first exclude the quiescent galaxies, which have no discernible PAH features (`qpah`<1) and a lack of ongoing star formation activity, such as ID:6823 shown in Fig. 6. Here `qpah` is the mass fraction of the PAH (Boquien et al. 2019). Some of these galaxies may correspond to foreground cluster members.

Then, we use the photometric redshift obtained from the `cigale` fit including MIRI to convert the best-fitting models to its rest frame wavelength. We perform a linear interpolation for each model, ranging from 0.1 to 20 microns. Next, we use the bootstrap

Downloaded from https://academic.oup.com/mnras/article/531/1/617/7675333 by Liverpool John Moores University user on 23 September 2024

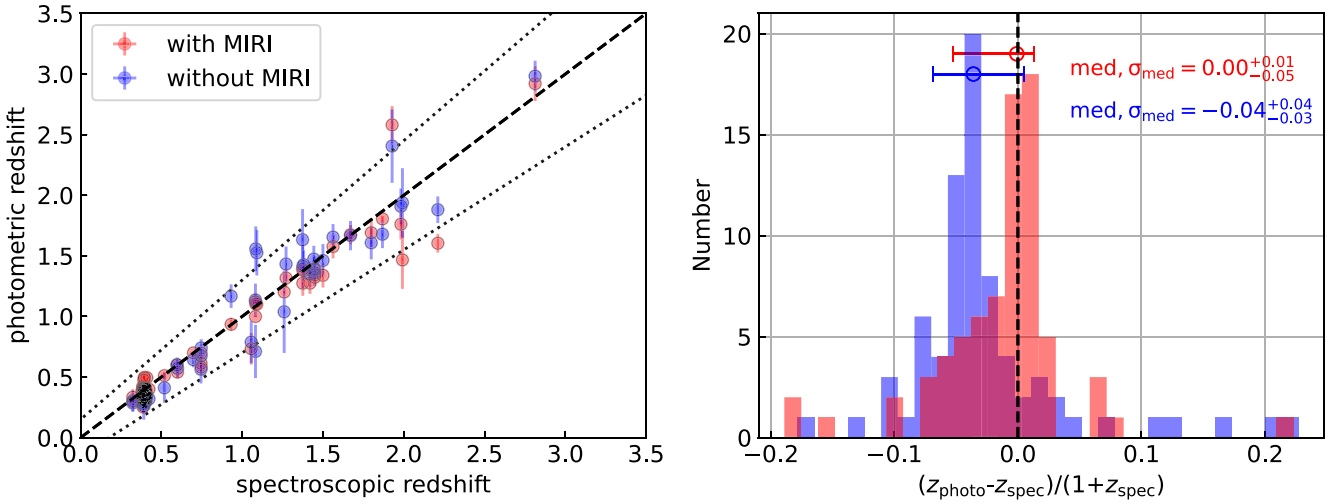

Figure 8. Left: Diagnostic plot showing the comparison of spectroscopic redshifts with photometric redshifts for fits with and without MIRI data. The spectroscopic redshifts are from the observations of Subaru, VLT/MUSE, JWST/NIRISS, and JWST/NIRSpec (Caminha et al. 2022; Carnall et al. 2023; Noirot et al. 2023). The black dashed line shows the one-to-one relation; the dotted lines show 15 per cent offsets in $(1 + z)$. Right: the histogram of the relative difference between the photometric redshifts from our `cigale` fits with or without MIRI and the spectroscopic redshift in $(1 + z_{spec})$. The labelled scatter indicates the median of the relative difference, respectively. The error bars show the range of the 16th−84th percentiles.

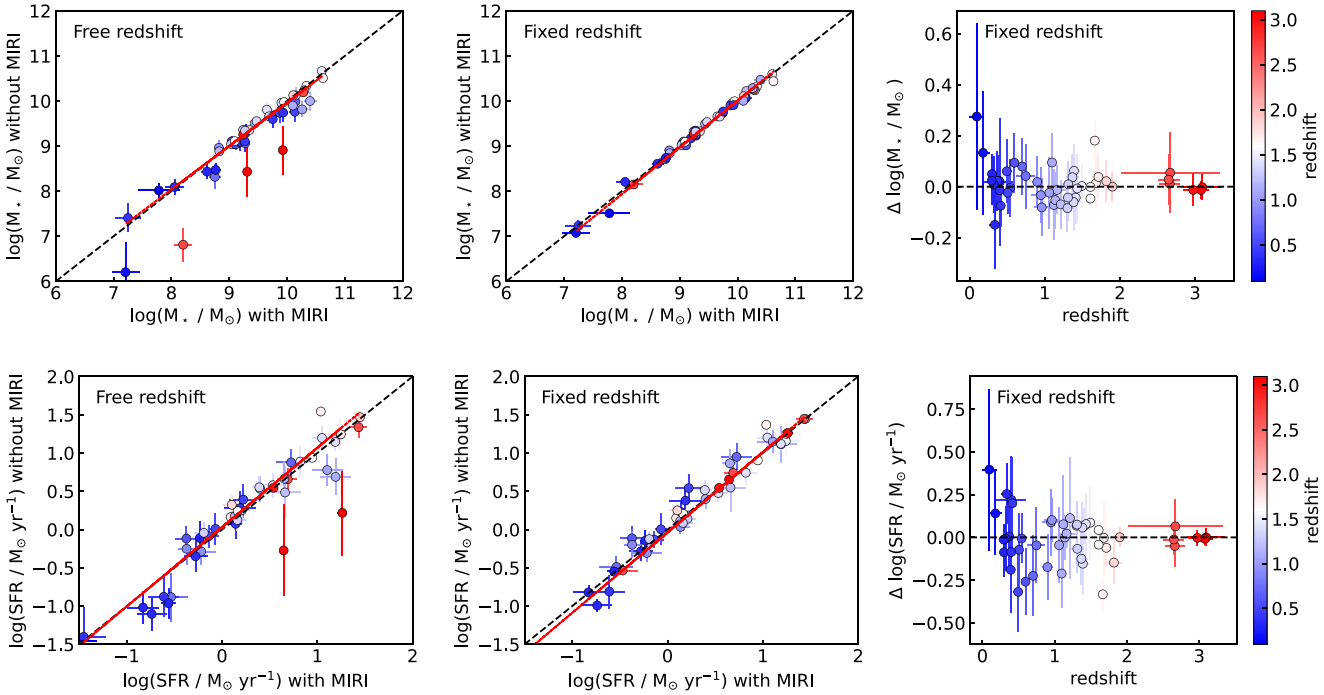

Figure 9. Comparisons between the derived stellar masses and star formation rates when including and excluding MIRI data. SFR and stellar masses are taken from the `cigale` SED fitting, as discussed in Section 3.1. The left-hand panel shows the comparisons of stellar masses and SFR respectively, when the redshift is a free parameter. The black dashed line shows the one-to-one relation, while the red line shows the best polyfitting considering the error. In the middle and right-hand panels, the redshifts are fixed to the values obtained from fitting the MIRI data. The right-hand panel shows the difference (Δ = X_{MIRI} - $X_{no\,MIRI}$) as a function of redshift. The colours of the points indicate the redshift. The stellar mass and SFR are corrected for magnification.

method to conduct 5000 repetitions calculating the median value and its error. Finally, we normalize the models at 3 microns, where the impact of emission lines and PAH can be avoided. We also employ a similar methodology to compute the median SED solely based on photometric data points, thereby mitigating the influence of fitting uncertainties. It is consistent in ensemble with that generated from the models.

Fig. 13 shows the median SED for both the AGN and SFG objects. The grey lines indicate each individually fitted model. The SEDs are relatively constant at wavelengths below approximately 4 μm. But

Downloaded from https://academic.oup.com/mnras/article/531/1/617/7675333 by Liverpool John Moores University user on 23 September 2024

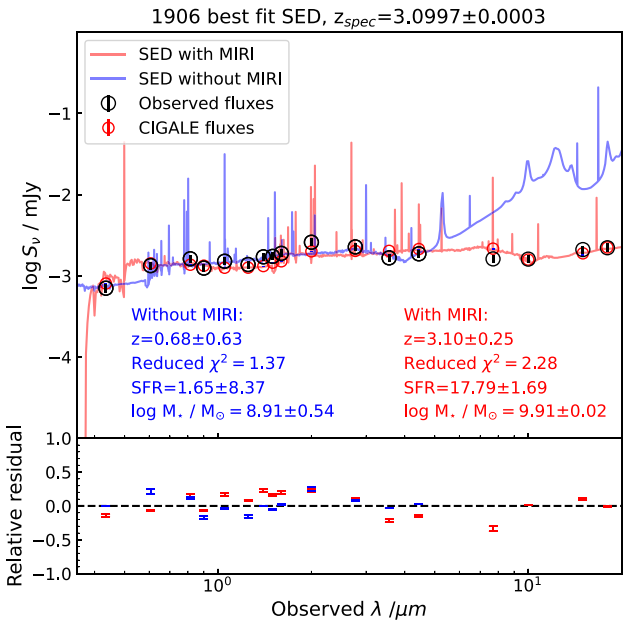

Figure 10. An example for different ways of fitting the SEDs in our sample. We show here the `cigale` SED fitting for Galaxy ID: 1906 with or without MIRI data. The black open circles are observed fluxes in each band; while the red ones are `cigale` Bayesian best fitting fluxes. The red and blue lines are the best-fitting SEDs with and without MIRI, respectively. The bottom panel is the relative residual of the observed data points and the fitting results. There are no blue points at long wavelengths as in this situation there is no data here.

the slope of the SEDs begins to change at longer wavelengths as a result of the presence of dust and AGN. It is evident that AGN and dust greatly contribute to the red wavelengths. At redshifts of z = 0–3.5, MIRI F770W corresponds to a rest wavelength of 2 − 8 μm, and F1800W corresponds to 4 − 18 μm. In this case, the MIRI data is responsible for fitting data larger than 2 μm. Note that we do not differentiate between different redshift bins due to a limited number of samples, but all our sample's photometric redshifts are less than 3.5. Thus, the results are not significantly impacted by a very wide redshift distribution and range.

We overlay on these SEDS a moderately luminous AGN – Seyfert 2 galaxy template[10] and a star-forming galaxy template. The MIRI-selected SFGs exhibit strong dust emission and prominent PAH features. Their median SED closely resembles that of typical starburst galaxies. The median AGN SED is similar to Seyfert 2 in the ensemble sense, but has lower 6–9 μm PAH emission. The 6–9 μm emission primarily arises from highly vibrationally excited cations, whereas the 3.3 μm, 8.6 μm, and 11.3 μm originate mostly from neutral PAH molecules (e.g. Allamandola et al. 1989; Li & Draine 2001; Draine et al. 2021).

The varying ratios, such as 6.2 μm or 7.7 μm/11.3 μm, indicate differences in the PAH ionization fraction (e.g. Galliano et al. 2008; Rigopoulou et al. 2021). AGN SEDs have a slightly lower average at 6.2 and 7.7 μm compared to SFGs. This suggests a lower fraction of ionized PAH molecules in AGN-dominated systems from within our sample. These findings align with a PAH study on Seyfert galaxies and SFGs using Spitzer/InfraRed spectral data in García-Bernete et al. (2022). They imply that the nuclear molecular gas concentration in AGN centers may play a role in shielding their PAH molecules.

We emphasize that our current MIRI data points only rely on broadband photometric data. This approach may omit PAH characteristic lines, leading to inadequate fitting. To address this limitation, MIRI medium-resolution spectrometer (MRS) can provide high-resolution spectra, enabling us to determine PAH characteristic lines and mid-infrared band physical parameters more accurately.

4.5 The impact of MIRI on median SED fitting

One of the things we investigate in this subsection is the impact of MIRI data on the overall shape and form of SEDs. What we are interested in examining is how different these SEDs would be with and without MIRI data. Fig. 14 shows the median SED and the difference when fitting the data with and without MIRI. The SED difference is not noticeable at wavelengths less than 4 microns. However, at longer wavelengths, including MIRI data leads to prominent PAH features compared to the case without it (Fig. 14 top panel). This is because the absence of MIRI data would make it impossible to constrain the PAH emission line details in mid-infrared bands. But the dust continuum exhibits a similarity between the two cases. The `cigale` fitting procedure guesses a relatively accurate model of dust emission, which aligns with the actual properties of the galaxies under investigation. Note the quiescent galaxies were excluded from the analysis due to their infrared SED shapes that deviate significantly from those of other galaxies.

At the rest wavelength between 4000 Å and 1 micron, we find that including MIRI data in the fitting process yields a slightly steeper optical slope, though the effect is less pronounced. We also investigate the SEDs shown in Fig. 14 (bottom), when it comes to light which is emitted at wavelengths less than 4000 Å . We calculate the rest-frame UV slope (β) by fitting a power-law model of the form $f_\lambda \propto \lambda^\beta$ to the UV photometry within the range 1250Å; $< \lambda_{\rm rest} <$ 3000Å; using SED fitting (Calzetti, Kinney & Storchi-Bergmann 1994; Bouwens et al. 2009; Finkelstein et al. 2012).

The best-fitting average UV slope with MIRI data is $\beta = -1.84 \pm 0.01$; whereas it is $\beta = -1.68 \pm 0.01$ without MIRI. This indicates that the MIRI selected galaxies exhibit bluer colours, lower levels of dust attenuation, and younger stellar populations. This finding is also pointed out in Papovich et al. (2023) for the CEERS field. It is important to note that the resolution of MIRI broadband photometry data points may not be sufficient to accurately identify key spectral lines, leading to inaccuracies in the existing median SED. In the future, further research using MIRI/MRS would improve our understanding of SED in the mid-infrared band.

5 CONCLUSIONS

In this eighth article of the EPOCHS series, we collect data from JWST/MIRI to analyse the field SMACS0723, which is the first public release of data from this instrument from JWST. In this study, we focus on the overlapping region between the MIRI, NIRCam, and HST observations, covering an area of approximately 2.3 arcmin^2. Within this region, we select 181 sources from a MIRI based catalogue and measure their photometric redshifts. Furthermore, we conduct an extensive investigation of various properties, including star formation activity, stellar mass, and contributions from AGNs. Our primary findings include:

(i) We use MIRI, NIRCam, and HST data to determine these galaxies' photometric redshifts of the range of z = 0–3.5. Furthermore,

[10]SWIRE Template Library: http://www.iasf-milano.inaf.it/~polletta/templates/swire_templates.html

Downloaded from https://academic.oup.com/mnras/article/531/1/617/7675333 by Liverpool John Moores University user on 23 September 2024

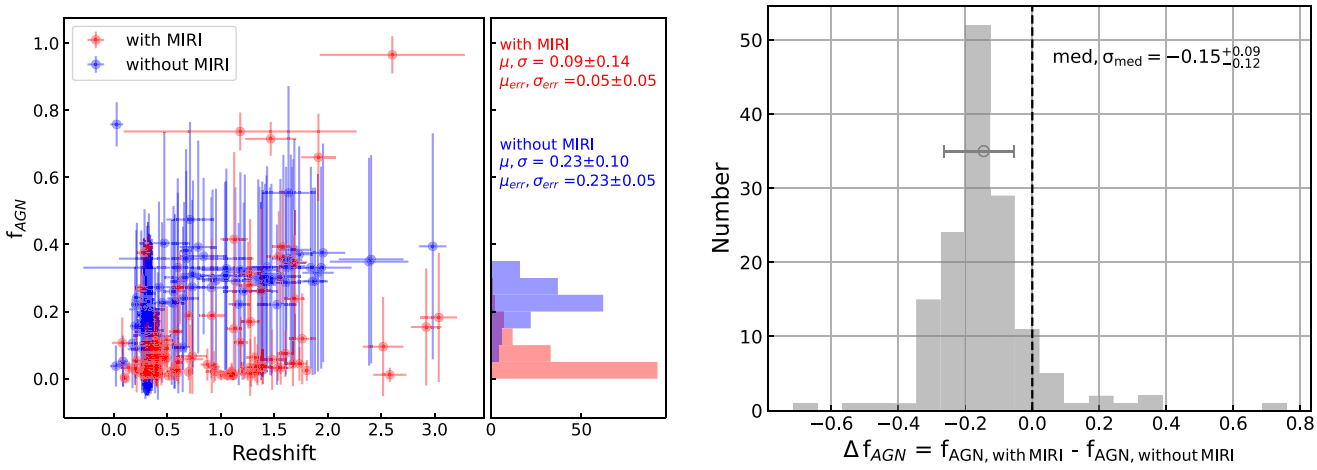

Figure 11. Left: The AGN fraction($\texttt{frac}_{\rm AGN}$) as a function of redshift with and without MIRI data. Right: the distribution of the difference $\texttt{frac}_{\rm AGN}$ (Δ $\rm frac_{AGN} = frac_{AGN,MIRI} - frac_{AGN,no\,MIRI}$) for galaxies with and without MIRI in the fits. The median value for this difference is $-0.15^{+0.09}_{-0.12}$, similar to what is found in the MIRISIM simulation of CEERS imaging (Yang et al. 2021), that find a value −0.2. The error bars show the range of the 16th−84th percentiles.

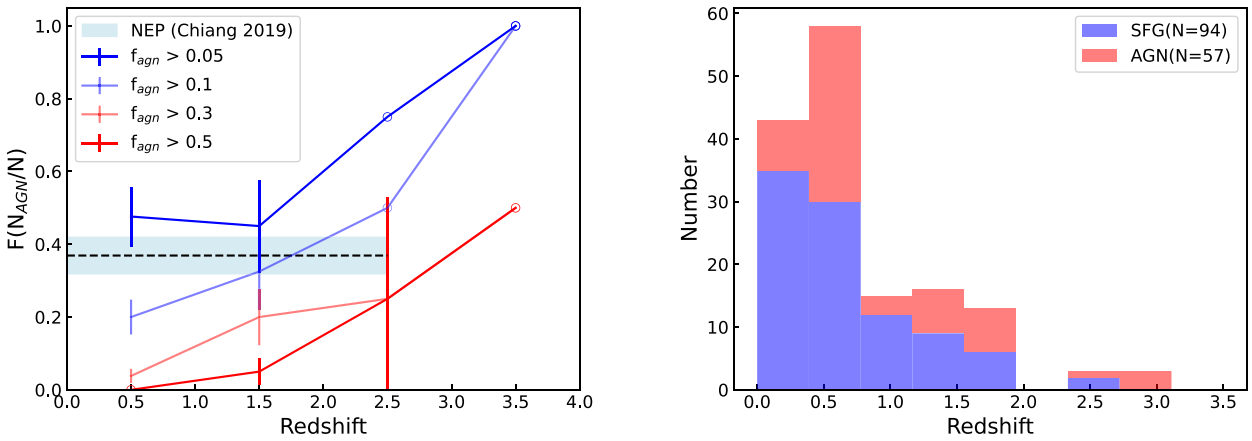

Figure 12. Left: The proportion of AGN to the total number of galaxies as a function of redshift. We compare different $\texttt{frac}_{\rm AGN}$ values [0.05, 0.1, 0.3, ≈nd 0.5]. We mark the points with significant uncertainty greater than 1 as open circles. With the NEP observational statistics (although these galaxies are at different redshifts and magnitudes), we conclude that a $\texttt{frac}_{\rm AGN}$ value of 0.1 is appropriate. The data shows that 37.7 per cent of the sample consists of AGN in this case. Therefore, we classify objects with $\texttt{frac}_{\rm AGN}$ values less than 0.1 as SFG and those above as AGN. Right: The redshift distribution of AGN and SFG is categorized based on this $\texttt{frac}_{\rm AGN}$ = 0.1 limit.

we conduct a detailed analysis of the stellar populations and the star formation and dust properties of each galaxy with and without the use of MIRI data

(ii) We conduct a comparison between the photometric redshifts obtained with and without MIRI data, and cross-check them with existing spectroscopic redshifts. We find the results of the photometric redshifts are in good agreement with spectroscopic redshifts. Including MIRI data leads to an small average 0.1 per cent difference between photometric and spectroscopic redshifts, while the difference is 4 per cent without MIRI data. Additionally, the fitting error has also been reduced by 20 per cent. The redshifts of three galaxies vary by as much as $\Delta z > 2$, and there are instances where high redshift galaxies would incorrectly be put at low-z without the use of MIRI data. The photometric redshifts with MIRI are highly consistent with spectroscopic redshifts, showing that the MIRI fits are better.

(iii) We compare stellar masses and SFRs measured with and without MIRI data. Including MIRI is consistent with stellar mass measurements obtained only from HST and NIRCAM, while the SFR is slightly reduced systematically by <0.1 dex. Moreover, MIRI data also led to a decrease in both parameter errors by an average of ∼0.1dex.

(iv) We select 151 the best-fitting galaxies ($\chi^2 < 6$) and categorize these using the parameter $\texttt{frac}_{\rm AGN}$, where we consider galaxies with $\texttt{frac}_{\rm AGN}$>0.1 as AGN. Out of the total samples, 37.7 per cent (57/151) are found to be AGN. We determine the median values for AGN and SFG, respectively. Our findings suggest that AGN and dust have a great impact on the long-wavelength flux, which is covered by the MIRI bands. Compared with the SED template, we find the SFGs match the starburst galaxy template very well. We also find that including MIRI data significantly reduces the mean value of $\texttt{frac}_{\rm AGN}$, to 0.09 ± 0.14, with its uncertainty also decreased of $\Delta\mu_{\rm err} = 0.18$.

Downloaded from https://academic.oup.com/mnras/article/531/1/617/7675333 by Liverpool John Moores University user on 23 September 2024

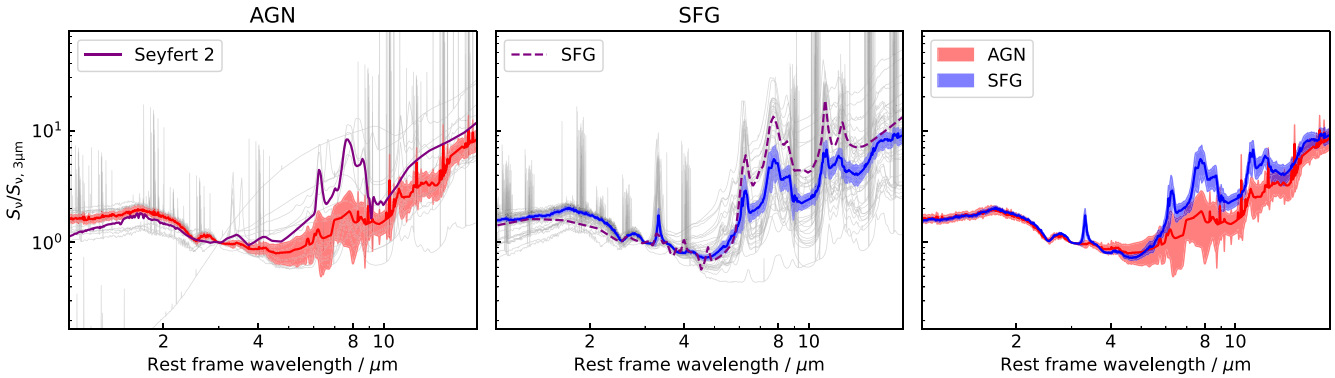

Figure 13. The median SEDs of AGN and SFGs fitting with MIRI using `cigale`. The gray lines indicate the individual robust fitting models, shifted to the rest-frame. The models are all normalized at 3 microns. The median SED and its error are obtained by sampling 5000 times using the bootstrap method. The purple solid line is a Seyfert 2 galaxy template from the SWIRE Template Library; the purple dashed line is the star-forming galaxy template. These templates are also normalized at 3 microns.

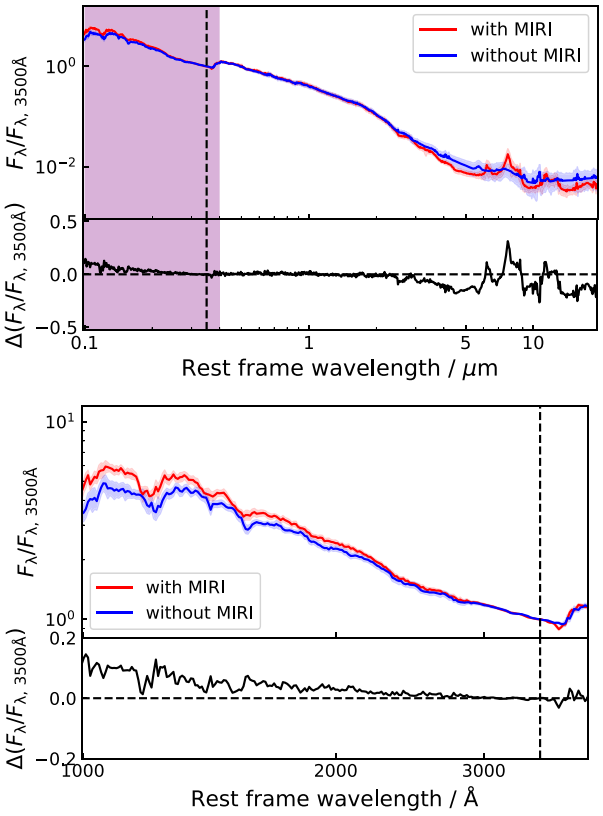

Figure 14. Comparison of median SEDs fitted when we include or exclude MIRI data. The SEDs have been normalized to 3500 Å , shown as the dashed line. The bottom panel is a zoom-in view in the range from 1000 to 4000 Å . The lower part of each panel shows the difference between best fit SEDs with or without MIRI data (X_{MIRI}-$X_{no\,MIRI}$), plotted as the black line.

(v) We compare the median SEDs of our sample with and without MIRI data. We find that at wavelengths greater than 4 μm, including MIRI data reveals significant PAH features, while the dust continuum remains similar. Including MIRI data yields steeper optical and UV slopes, indicating bluer colours, lower dust attenuation, and younger stellar populations.

At present, the MIRI observations remain relatively shallow, with an average depth approximately 3 mag shallower than that of NIRCam in the SMACS0723 field. Extending the depth of MIRI observations in the future will open up a promising avenue to explore the intricacies of these galaxies in detail, and to enable the discovery of fainter and hidden galaxies. Moreover, future research utilising MIRI/MRS will improve comprehension of SEDs in the mid-infrared band and offer a more efficient approach to get redshifts and star formation rates. Through combining this with spectroscopic observations, a more detailed and nuanced illustration of the galaxies' emissions, dust properties, and other significant attributes can be achieved.

ACKNOWLEDGEMENTS

QL, CC, JT, and NA acknowledge support from the ERC Advanced Investigator Grant EPOCHS (788113). DA and TH acknowledge support from STFC in the form of PhD studentships.

This work is based on observations made with the NASA/ESA *Hubble Space Telescope* (HST) and NASA/ESA/CSA *JWST* obtained from the `Mikulski Archive for Space Telescopes` (`MAST`) at the *Space Telescope Science Institute* (STScI), which is operated by the Association of Universities for Research in Astronomy, Inc., under NASA contract NAS 5–03127 for JWST, and NAS 5–26555 for HST. The observations used in this work are associated with JWST program 2736. The authors thank all involved in the construction and operations of the telescope as well as those who designed and executed these observations.

The authors thank Anthony Holloway and Sotirios Sanidas for their providing their expertise in high performance computing and other IT support throughout this work. This work makes use of ASTROPY (Astropy Collaboration et al. 2013, 2018, 2022), MATPLOTLIB (Hunter 2007), REPROJECT, DRIZZLEPAC, SCIPY (Virtanen et al. 2020), and PHOTUTILS (Bradley et al. 2022).

DATA AVAILABILITY

The JWST data used in this work are available in the Early Release Observations (ERO) programme (ID: 2736, PI: K. Pontoppidan, Pontoppidan et al. 2022) through the Mikulski Archive for Space Telescopes (https://mast.stsci.edu/). HST data of SMACS0723 from the Reionization Lensing Cluster Survey (RELICS; ID: GO 14017; Coe et al. 2019) used in this article will be shared on reasonable

Downloaded from https://academic.oup.com/mnras/article/531/1/617/7675333 by Liverpool John Moores University user on 23 September 2024

request to Dan Coe. Additional data products will be shared on reasonable request to the first author.

REFERENCES

Adams N. J. et al., 2023, MNRAS, 518, 4755
Allamandola L. J., Tielens A. G. G. M., Barker J. R., 1989, ApJS, 71, 733
Álvarez-Márquez J. et al., 2023, A&A, 671, A105
Asboth V. et al., 2016, MNRAS, 462, 1989
Ashby M. L. N. et al., 2015, ApJS, 218, 33
Astropy Collaboration et al., 2013, A&A, 558, A33
Astropy Collaboration et al., 2018, AJ, 156, 123
Astropy Collaboration et al., 2022, ApJ, 935, 167
Barro G. et al., 2024, ApJ, 963, 128
Bertin E., Arnouts S., 1996, A&AS, 117, 393
Bertin E., Schefer M., Apostolakos N., Álvarez-Ayllón A., Dubath P., Kümmel M., 2022, Astrophysics Source Code Library. record ascl:2212.018
Boquien M., Burgarella D., Roehlly Y., Buat V., Ciesla L., Corre D., Inoue A. K., Salas H., 2019, A&A, 622, A103
Bouwens R. J. et al., 2009, ApJ, 705, 936
Bouwens R. J. et al., 2023, MNRAS, 523, 1036
Bradley L., et al., 2022, Zenodo,
Brammer G. B., van Dokkum P. G., Coppi P., 2008, ApJ, 686, 1503
Bruzual G., Charlot S., 2003, MNRAS, 344, 1000
Calzetti D., Kinney A. L., Storchi-Bergmann T., 1994, ApJ, 429, 582
Calzetti D., Armus L., Bohlin R. C., Kinney A. L., Koornneef J., Storchi-Bergmann T., 2000, ApJ, 533, 682
Caminha G. B., Suyu S. H., Mercurio A., Brammer G., Bergamini P., Acebron A., Vanzella E., 2022, A&A, 666, L9
Carnall A. C. et al., 2023, MNRAS, 518, L45
Castellano M. et al., 2022, ApJ, 938, L15
Chabrier G., 2003, PASP, 115, 763
Chiang C.-Y., Goto T., Hashimoto T., Kim S. J., Matsuhara H., Oi N., 2019, PASJ, 71, 31
Coe D. et al., 2019, ApJ, 884, 85
Donnari M., Pillepich A., Nelson D., Marinacci F., Vogelsberger M., Hernquist L., 2021, MNRAS, 506, 4760
Draine B. T., 2003, ARA&A, 41, 241
Draine B. T., Li A., 2007, ApJ, 657, 810
Draine B. T. et al., 2014, ApJ, 780, 172
Draine B. T., Li A., Hensley B. S., Hunt L. K., Sandstrom K., Smith J. D. T., 2021, ApJ, 917, 3
Ebeling H., Edge A. C., Mantz A., Barrett E., Henry J. P., Ma C. J., van Speybroeck L., 2010, MNRAS, 407, 83
Endsley R., Stark D. P., Whitler L., Topping M. W., Chen Z., Plat A., Chisholm J., Charlot S., 2023, MNRAS
Ferreira L. et al., 2022, ApJ, 938, L2
Finkelstein S. L. et al., 2012, ApJ, 756, 164
Fritz J., Franceschini A., Hatziminaoglou E., 2006, MNRAS, 366, 767
Fudamoto Y. et al., 2017, MNRAS, 472, 2028
Galliano F., Madden S. C., Tielens A. G. G. M., Peeters E., Jones A. P., 2008, ApJ, 679, 310
García-Bernete I., Rigopoulou D., Alonso-Herrero A., Pereira-Santaella M., Roche P. F., Kerkeni B., 2022, MNRAS, 509, 4256
Golubchik M., Furtak L. J., Meena A. K., Zitrin A., 2022, ApJ, 938, 14
Harikane Y. et al., 2022, ApJ, 929, 1
Hunter J. D., 2007, Comput. Sci. Eng., 9, 90
Juodžbalis I. et al., 2023, MNRAS, 525, 1353
Kim K. J. et al., 2023, ApJ, 955, 32
Kirkpatrick A. et al., 2023, ApJ, 959, L7
Kotilainen J. K., Ward M. J., Boisson C., Depoy D. L., Smith M. G., 1992, MNRAS, 256, 149
Kroupa P., 2001, MNRAS, 322, 231
Lagattuta D. J. et al., 2022, MNRAS, 514, 497
Langeroodi D., Hjorth J., 2023, ApJ, 946, L40
Larson R. L. et al., 2023, ApJ, 958, 141
Leitherer C., Li I. H., Calzetti D., Heckman T. M., 2002, ApJS, 140, 303
Li A., 2020, Nat. Astron., 4, 339
Li A., Draine B. T., 2001, ApJ, 554, 778
Lyu J. et al., 2023, preprint (arXiv:2310.12330)
Mahler G. et al., 2023, ApJ, 945, 49
McKay S. J., Barger A. J., Cowie L. L., Bauer F. E., Rosenthal M. J. N., 2023, ApJ, 951, 48
Medezinski E. et al., 2007, ApJ, 663, 717
Menzel M. et al., 2023, PASP, 135, 058002
Naidu R. P. et al., 2022, ApJ, 940, L14
Nayyeri H. et al., 2018, ApJS, 234, 38
Nenkova M., Sirocky M. M., Nikutta R., Ivezić Ž., Elitzur M., 2008, ApJ, 685, 160
Neugebauer G., Matthews K., 1999, AJ, 118, 35
Noirot G. et al., 2023, MNRAS
Oke J. B., Gunn J. E., 1983, ApJ, 266, 713
Papovich C. et al., 2023, ApJ, 949, L18
Pontoppidan K. M. et al., 2022, ApJ, 936, L14
Repp A., Ebeling H., 2018, MNRAS, 479, 844
Reuter C. et al., 2020, ApJ, 902, 78
Rich J. et al., 2023, ApJ, 944, L50
Richard J. et al., 2021, A&A, 646, A83
Rieke G. H. et al., 2015, PASP, 127, 584
Rigby J. et al., 2023, PASP, 135, 048001
Rigopoulou D. et al., 2021, MNRAS, 504, 5287
Schlafly E. F., Finkbeiner D. P., 2011, ApJ, 737, 103
Sellgren K., Werner M. W., Dinerstein H. L., 1983, ApJ, 271, L13
Sharon K., Chen M. C., Mahler G., Coe D., RELICS: Reionization Lensing Cluster Survey, 2023, ApJS, 264, 15
Siebenmorgen R., Heymann F., Efstathiou A., 2015, A&A, 583, A120
Stalevski M., Fritz J., Baes M., Nakos T., Popović L. Č., 2012, MNRAS, 420, 2756
Stalevski M., Ricci C., Ueda Y., Lira P., Fritz J., Baes M., 2016, MNRAS, 458, 2288
Sun F. et al., 2021, ApJ, 922, 114
Sun F. et al., 2022, ApJ, 932, 77
Timlin J. D. et al., 2016, ApJS, 225, 1
Villa-Vélez J. A., Buat V., Theulé P., Boquien M., Burgarella D., 2021, A&A, 654, A153
Virtanen P. et al., 2020, Nat. Methods, 17, 261
Weedman D. et al., 2006, ApJ, 653, 101
Wright G. S. et al., 2023, PASP, 135, 048003
Yan H., Ma Z., Ling C., Cheng C., Huang J.-S., 2023, ApJ, 942, L9
Yang G. et al., 2020, MNRAS, 491, 740
Yang G. et al., 2021, ApJ, 908, 144
Yang G. et al., 2022, ApJ, 927, 192
Yang G. et al., 2023, ApJ, 950, L5
Ysard N., Koehler M., Jimenez-Serra I., Jones A. P., Verstraete L., 2019, A&A, 631, A88

This paper has been typeset from a TEX/LATEX file prepared by the author.

Downloaded from https://academic.oup.com/mnras/article/531/1/617/7675333 by Liverpool John Moores University user on 23 September 2024

© 2024 The Author(s).
Published by Oxford University Press on behalf of Royal Astronomical Society. This is an Open Access article distributed under the terms of the Creative Commons Attribution License (https://creativecommons.org/licenses/by/4.0/), which permits unrestricted reuse, distribution, and reproduction in any medium, provided the original work is properly cited.